

Structural and Redox Properties of Ceria in Alumina-Supported Ceria Catalyst Supports

A. Martínez-Arias,* M. Fernández-García, L. N. Salamanca, R. X. Valenzuela, J. C. Conesa, and J. Soria

Instituto de Catálisis y Petroleoquímica, CSIC, Camino de Valdelatas s/n. Campus UAM, 28049 Madrid, Spain

Received: August 9, 1999; In Final Form: February 14, 2000

Several alumina-supported ceria samples with varying ceria contents (1, 2, 10, and 39 wt %) have been studied by different techniques (XRD, Raman, TEM-EDS, UV-vis DRS, XANES, and EPR), aiming to establish a complete model on the structural and redox characteristics of ceria entities in these samples. Two general types of ceria entities are observed: aggregated crystalline ceria species (3D-Ce) and dispersed ceria species in the form of two-dimensional patches (2D-Ce). The relative amounts of each of these species do not show a linear relationship with the cerium loading: as the cerium content is increased, a trend toward formation of 3D-Ce, to the detriment of 2D-Ce, is observed. The EPR data evidence differences in chemical (redox) behavior between 2D-Ce, 3D-Ce, and unsupported ceria. Thus, the main differing characteristic of some 3D-Ce particles with respect to unsupported ceria, which holds true for all 3D-Ce formed with weight percent ≤ 10 , is the absence of associated vacancies upon outgassing at 773 K (evidenced by EPR of chemisorbed oxygen). This behavior is attributed to the existence of an epitaxial relationship between ceria and the underlying alumina, which influences largely the properties of relatively small 3D-Ce particles. In the initial calcined state, 2D-Ce patches are shown to present cerium in a (formally) Ce^{4+} oxidation state, with relaxed coordination distances and experiencing a decreased ligand field which facilitates their reduction (in comparison with 3D-Ce or unsupported ceria). Implications of these results on molecular design of depollution catalysts are discussed.

Introduction

Alumina-supported ceria forms part of the so-called classical three-way catalysts (TWCs), used for the elimination of pollutants in automobile exhausts; it constitutes the active part of the support, onto which precious metals (usually Rh, Pt and/or Pd) are dispersed.¹ It is widely accepted that optimum catalytic performance of the system largely depends on the synergic interactions established between the precious metals and the ceria components of the catalyst, ceria acting as a catalytic activity promoter.¹ The promoting effects of ceria in these catalysts can be classified in two general types. First, it works as a structural promoting component, enhancing metal dispersion and participating to a certain extent in the stabilization of the alumina support toward thermal sintering.² Second, as a chemical promoter it enhances the oxygen storage capacity (OSC) of the catalyst, related to the particular ability of CeO_2 to undergo deep and rapid reduction/oxidation cycles according to the reaction $\text{CeO}_2 \leftrightarrow \text{CeO}_{2-x} + x/2\text{O}_2$ upon interaction with reducing or oxidizing components present in the reactant mixtures.³ Additionally, ceria can directly participate in the water–gas shift reaction⁴ or in the decomposition of nitrogen oxides.⁵ The extent of these effects largely depends on the metal–support interactions established between both metal and ceria components.^{6–8} In turn, these are expected to be largely influenced by the different physicochemical properties achieved by both the metals and the ceria components in the catalyst as a consequence of changes in their respective morphologies. Accordingly, recent works have shown that changes in the ceria morphology can strongly affect the redox properties of supported

metal catalysts, producing as a consequence significant differences in their catalytic performances.^{9–11} From a more practical point of view, a recent report has shown the importance of achieving a precise control of the metal–support interactions in order to obtain optimum catalytic systems in the case of so-called Pd-only TWCs (i.e. containing only palladium as active metal, in addition to OSC components—ceria related compounds—and alumina).¹² It has been shown that when palladium is applied in close contact with the OSC component, the catalyst achieves the exhaust emission standards proposed by the EU for 2000–2001 (Euro3 test), in contrast with a catalyst of similar composition, for which a more conventional preparation method with less control of the metal–support interactions was followed. Further improvement of these properties can probably be attained if a better knowledge of the characteristics of ceria entities present in these systems is achieved.

In this respect, the ceria entities that could be present in alumina-supported ceria systems can possibly be classified according to their different dispersion degrees.^{13–15} This leads to differentiate roughly between (i) dispersed ceria entities, which could in principle include isolated cerium ions, clusters thereof and/or more or less thick CeO_x patches (or 2D-Ce entities) and (ii) nondispersed ceria species (i.e. ceria aggregates or 3D-Ce entities). The formation and properties of the dispersed ceria entities are expected to depend strongly on the interactions established with the underlying alumina support, while, on the contrary, ceria aggregates are expected to present properties closer to those of unsupported ceria entities. A literature survey shows that, in general terms, the difficulty of characterizing these entities increases with their dispersion degree. Thus, aggregated ceria entities in supported ceria systems have been more or less well characterized, within the limits of each technique, by

* To whom correspondence should be sent. E-mail: amartinez@icp.csic.es.
Fax: 34 91 5854760.

different experimental techniques such as TEM,¹⁶ XRD,¹⁴ Raman,¹³ XPS,¹³ and UV-vis DRS.^{14,16} However, dispersed ceria entities have generally been characterized only in an indirect way (i.e., considering the lack or insufficient intensity of features due to aggregated ceria entities in ceria-containing samples) or by utilizing probe molecules. In this latter respect, features in the H₂-TPR profiles of several CeO₂/γ-Al₂O₃ samples, different from those observed for unsupported ceria, have been attributed to dispersed ceria species.¹³ Other works have shown differing acid-base properties when comparing supported and unsupported ceria systems, which have been attributed to the presence of dispersed ceria entities in the supported systems.^{14,17} Perhaps a higher level of details has been obtained by EPR using O₂ as a probe molecule, since it has differentiated cerium sites within dispersed ceria entities.¹⁵ On the other hand, the presence of a group of peaks at wavenumbers significantly different from that shown by crystalline cerium oxide in the Raman spectrum of a certain CeO₂/γ-Al₂O₃ sample has been proposed to arise from dispersed ceria entities. However, as recognized by the authors of that report, important doubts exist with respect to its possible attribution to transitional alumina phases generated by thermal treatments.¹³

To rationalize all these aspects, this work aims at establishing a clearer model of the characteristics of the ceria entities present in CeO₂/γ-Al₂O₃ samples typically used as catalyst supports.^{9–11} For this purpose, a multitechnique approach using XRD, Raman, UV-vis DRS, TEM-EDS, XANES, and EPR techniques is employed.

Experimental Section

Materials. Alumina-supported ceria samples were prepared by incipient wetness impregnation of a γ-Al₂O₃ support (supplied by Condea and showing $S_{\text{BET}} = 200 \text{ m}^2 \text{ g}^{-1}$) with aqueous solutions of Ce(NO₃)₃·6H₂O. Following impregnation, the samples were dried at 383 K for 24 h and finally calcined in dry air for 2 h at 773 K. The cerium oxide loadings of the thus prepared samples range from 1 to 39 wt % (i.e. from 0.03 to 1.5 theoretical ceria monolayers). Hereafter, they will be referred to as samples *x*CA, where *x* denotes the ceria weight percentage present in each sample. CeO₂ (referred to as sample C) was supplied by Rhône-Poulenc and showed $S_{\text{BET}} = 103 \text{ m}^2 \text{ g}^{-1}$. A reference CeAlO₃ sample was prepared by a freeze-drying method using aqueous solutions of aluminum and cerium nitrates and calcining the mixture in air at 1573 K until CeAlO₃ was obtained, verified by the exclusive presence of narrow peaks in the X-ray diffractogram, corresponding to this perovskite phase.

Techniques. Powder XRD patterns were recorded on a Seifert diffractometer using nickel-filtered Cu Kα radiation operating at 40 kV and 40 mA and with a 0.03° step size.

Raman spectra were obtained at room temperature with a Bruker RFS-100 FT-Raman spectrometer provided with a diode-pumped germanium solid-state detector, which operates at liquid N₂ temperature. A Nd:YAG laser was used as exciting source. The samples were ground to fine powders and pressed into the holder with no other pretreatment. A laser power of ca. 10 mW was typically used, the spectra being taken with a resolution of 4 cm⁻¹ and accumulating 100 scans.

UV-visible diffuse reflectance spectroscopy (DRS) experiments were performed with a Shimadzu UV2100 spectrometer. The Kubelka-Munk function was used to present all the spectra.

Samples for transmission electron microscopy (TEM) were prepared by crushing the materials in an agate mortar, dispersing ultrasonically in isobutyl alcohol, and depositing on perforated

carbon films supported on copper grids. TEM data were obtained on a JEOL 2000 FX II system (with 3.1 Å point resolution) equipped with a LINK probe for energy dispersive spectroscopy (EDS) analysis. Several portions of the materials were examined at low magnifications performing simultaneous EDS analyses (using an incident electron beam diameter of 500 nm). Electron diffractograms, micrographs, and dark-field images (the latter obtained using rings corresponding to the ceria (111) and (200) spacings) were recorded over selected areas of the samples with compositions previously characterized by EDS. The diffraction images were digitized with a scanner and subjected to computer densitometry with in-house software to yield (angle-integrated) radial profiles.

X-ray absorption near-edge spectroscopy (XANES) data at the L_{III}-edge of Ce were obtained on the BM-29 Line at ESRF. A double-crystal Si(311) monochromator with an estimated resolution of 0.5 eV was used. The harmonic content of the beam was minimized by a 50% detuning of the crystals. All samples (self-supported wafers with thicknesses giving an absorbance of ca. 2.0) were measured in a transmission mode at liquid nitrogen temperature and with simultaneous calibration of the energy scale against a CeO₂ reference.

EPR spectra were recorded at 77 K with a Bruker ER 200 D spectrometer operating in the X-band and calibrated with a DPPH standard ($g = 2.0036$). Portions of about 40 mg of the sample were placed inside a quartz probe cell with greaseless valves using a conventional high vacuum line (capable of maintaining a dynamic vacuum of ca. 0.006 N m⁻²) for the different treatments. The samples were in all cases pretreated in the EPR cell with 300 Torr of pure O₂ at 773 K, followed by thorough outgassing at room temperature. The procedure employed for the EPR oxygen adsorption experiments was as follows: first, the sample was outgassed at 773 K for 2 h (a 5 K min⁻¹ ramp being applied); then, after cooling to room temperature, the EPR cell is immersed into liquid N₂, and about 200 μmol of O₂ per gram of sample is admitted into the cell, allowing about 15 min of contact with oxygen and subsequently outgassing for 30 min. Finally, the sample was warmed to room temperature during 30 min and subsequently cooled again with liquid nitrogen for recording the spectrum.

Results

XRD. Figure 1 shows the X-ray diffractograms of the samples. The diffractogram of sample C can be indexed according to its stable cubic fluorite structure (space group *Fm3m*). Similar peaks due to ceria are observed for samples 39CA and 10CA, with overall increasing width (suggesting decreasing average particle sizes) and decreasing intensity as the ceria loading is decreased. On the other hand, ceria peaks are absent in the diffractograms of samples 1CA and 2CA, which present only peaks due to γ-Al₂O₃.¹⁴

Raman. Figure 2 displays the Raman spectra of the samples. Sample C shows a strong peak at 462 cm⁻¹ due to the F_{2g} Raman-active mode characteristic of the fluorite structure of CeO₂. Besides, it shows a weak band at around 260 cm⁻¹ and a shoulder at ca. 600 cm⁻¹, which have been attributed respectively to the normally Raman inactive (but IR active) transverse and longitudinal optical phonon modes at the Brillouin zone center.¹³ The presence of these latter peaks might be due to perturbations of the fluorite structure. The peak at 462 cm⁻¹ is also present in samples 39CA and 10CA, its intensity decreases upon decreasing the amount of ceria present in the sample, but it is not detected for samples 2CA and 1CA. A nonlinear character is observed between the amount of ceria

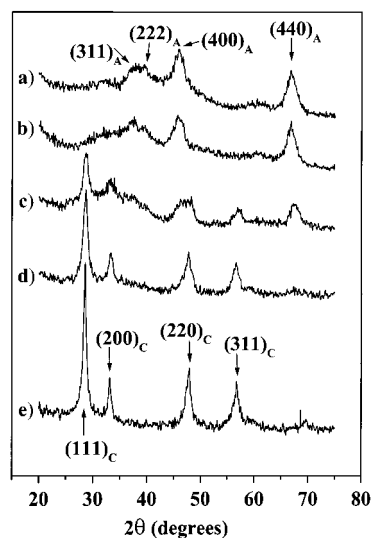


Figure 1. X-ray diffractograms of (a) 1CA, (b) 2CA, (c) 10CA, (d) 39CA, and (e) C samples. A and C subindexes refer to γ - Al_2O_3 and ceria, respectively.

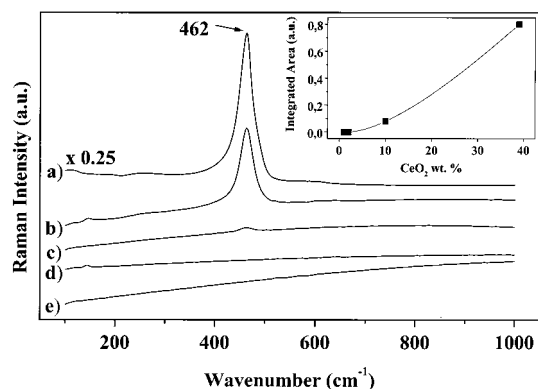


Figure 2. Raman spectra of (a) C, (b) 39CA, (c) 10CA, (d) 2CA, and (e) 1CA samples. The inset shows the integrated area of the Raman band at 462 cm^{-1} as a function of the ceria loading.

TABLE 1: Ce/Al Atomic Ratio Obtained by TEM-EDS

sample	Ce/Al
1CA	4×10^{-3}
2CA	$(5 \times 10^{-3}) - (7 \times 10^{-3})$
10CA	$(2 \times 10^{-2}) - (2 \times 10^{-1})$
39CA	$(6 \times 10^{-3}) - 1$

present in samples x CA and the integrated area of the peak at 462 cm^{-1} , as shown in the inset of Figure 2. No other peaks different from that at 462 cm^{-1} were detected in the spectra of x CA samples, in contrast with previous results on other alumina-supported ceria samples, displaying a different group of peaks which were tentatively ascribed to dispersed ceria species.¹³

TEM. The EDS results (Table 1) and the electron diffraction study (Figure 3) evidence an increasing (morphological) heterogeneity of the x CA materials with increasing cerium content. 1CA and 2CA show very low Ce/Al atomic ratios, close to the ones expected for the corresponding Ce loadings. Practically no variation is observed in the Ce/Al atomic ratio throughout the set of aggregates (6–10) inspected by TEM/EDS for these two samples. No diffraction lines attributable to cerium compounds are, on the other hand, detected in any of both cases. For 10CA, the Ce/Al ratio ranges in 1 order of magnitude, with the values depending on the zone analyzed, although in all cases quite similar diffraction profiles (only differing in their respective intensities) are obtained. Concerning cerium-related lines,

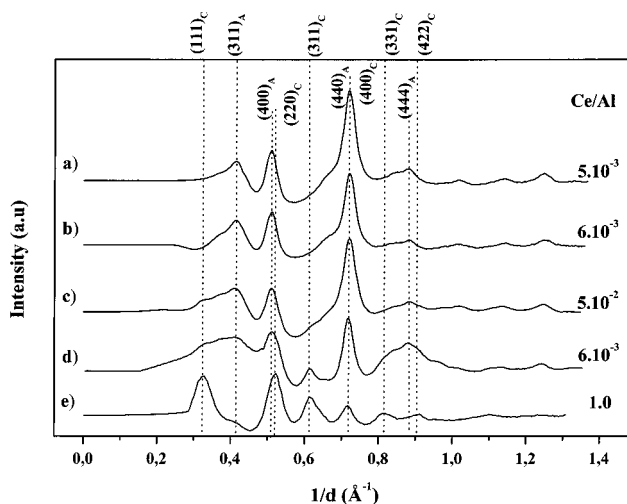


Figure 3. Radial (angle averaged) densitometry patterns of the electron diffraction rings observed in specific zones of the 1CA (a), 2CA (b), 10CA (c), and 39CA (d, e) samples. Ce/Al atomic ratios determined by EDS are included in the figure. Vertical dashed lines mark the strongest reflections of ceria and alumina (subindexed as C and A, respectively).

only the strongest one of ceria, i.e., (111), appears clearly visible in the corresponding diffractogram, displayed in Figure 3. The average CeO_2 particle size in 10CA, measured from dark-field images (Figure 4a), is close to 6 nm. The morphological heterogeneity grows markedly from the 10CA to the 39CA specimen, the latter clearly containing both Al- and Ce-enriched zones. Interesting to note is the fact that, not depending on the zone (either Al or Ce enriched), the diffraction pattern of 39CA shows contributions from well-developed CeO_2 particles (Figure 3d,e). In fact, dark-field images of the Al-rich zone (Figure 4b) allow one to estimate average ceria particle sizes of 11 nm, while the Ce-rich zones contain ceria particles (often identifiable as single crystallites) with sizes of a few hundreds of nanometers.

DRS. Spectra in the 200–500 nm range of unsupported ceria, alumina, and several x CA samples are shown in Figure 5. A featureless spectrum is obtained for alumina in the examined range (curve a). The two maxima shown by unsupported ceria have been interpreted as being due to specular reflectance effects (produced by the strong absorption of ceria in the UV range) affecting the shape of the interband transition, although not modifying the absorption edge position which appears at ca. 400 nm.¹⁶ In the case of x CA samples, the absorption edge is blue-shifted with respect to unsupported ceria and its wavelength decreases with decreasing cerium content. A similar decrease is produced also in the position of the absorption maximum, at least for the samples with lower Ce content (in the 39CA sample, a hint of a two-component structure might be due to specular effects similar, although less marked, to those of CeO_2). According to previous studies,^{16,18} two possible interpretations can be given for these results. Thus, considering quantum size effects, the blue shift in the absorption edge (corresponding to interband transitions) would be produced as a consequence of decreasing the ceria particle size. On the other hand, localized effects due to increasing contributions of Ce^{4+} –oxygen charge transfer transitions (which predominate in the presence of small crystallites with a high surface/volume ratio, yielding a relatively broad band at ca. 280 nm),¹⁸ might also produce similar results as the ceria loading decreases.

XANES. Normalized XANES spectra of sample 2CA (chosen to optimally observe the most dispersed ceria species) and of

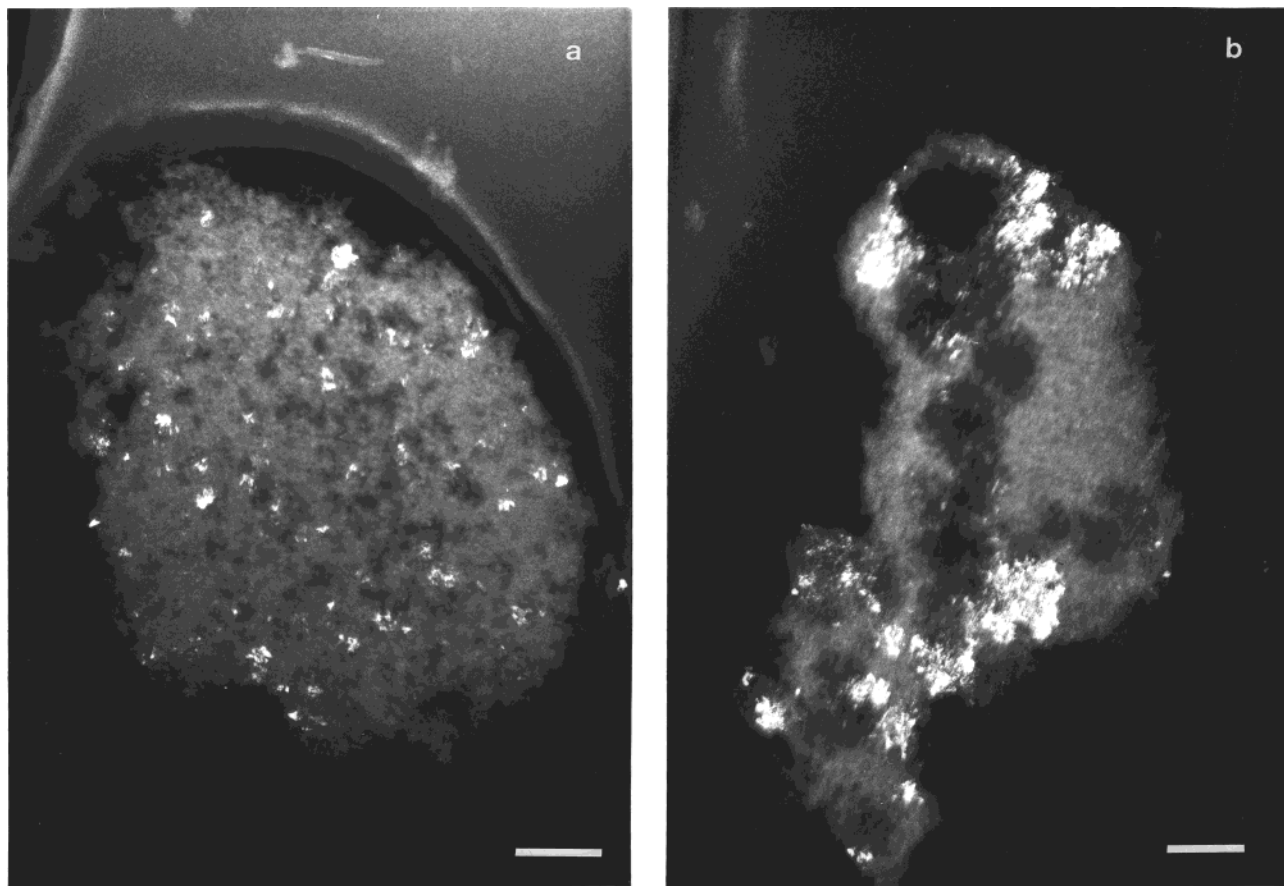


Figure 4. Dark-field TEM images of (a) 10CA and (b) 39CA samples. Both horizontal scales correspond to 100 nm.

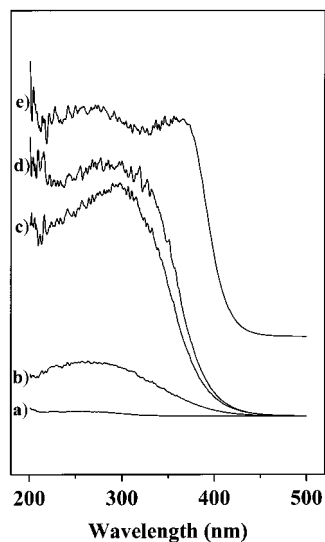


Figure 5. UV-vis DRS spectra of (a) alumina, (b) 1CA, (c) 10CA, (d) 39CA, and (e) C samples.

samples CeAlO_3 and C (used as references for the Ce^{3+} and Ce^{4+} states, respectively) are shown in Figure 6. No analysis of EXAFS data was carried out, as the signal-to-noise ratio in such a low-loading sample was insufficient. The XANES spectra show, close to the absorption edge, the strong features (known as “white line(s)”) due to excitation of the 2p core level into the bound 5d orbitals; these are followed above 5750 eV by the first continuum resonance (CR), i.e., excitation into an unbound state, which in the CeO_2 case is dominated by a mixture of contributions to the final state by Ce(f) and O(d) orbitals from the second and further coordination shells.^{19,20}

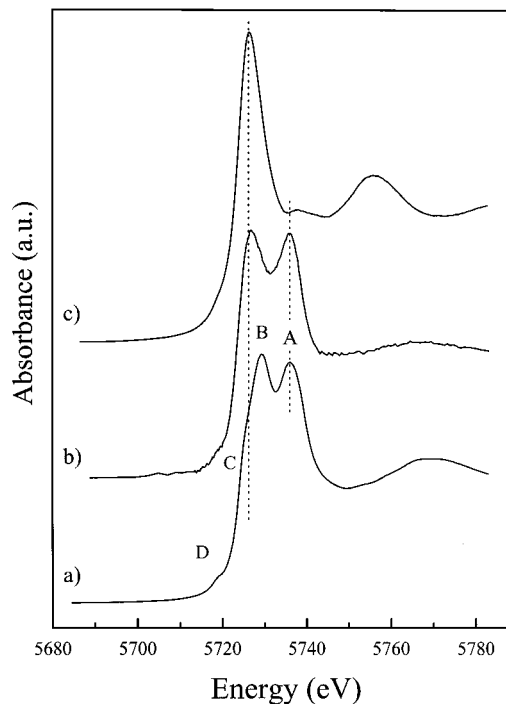


Figure 6. Ce L_{III}-edge XANES spectra of (a) CeO_2 , (b) 2CA, and (c) CeAlO_3 . See the text for details concerning peak assignments.

The CeAlO_3 XANES shape is dominated by a single white line, characteristic of Ce^{3+} , located at ca. 5726 eV, and ascribed to a $\{\text{Ce}2p^{5.4}f^{1.5}d^{*1}, \text{O}2p^6\}$ final state.^{19,20} In contrast, the CeO_2 reference (sample C) exhibits a complex white line shape with four different lines that have been denoted as A, B, C, and D in recent literature.²⁰ After some debate, it has been established

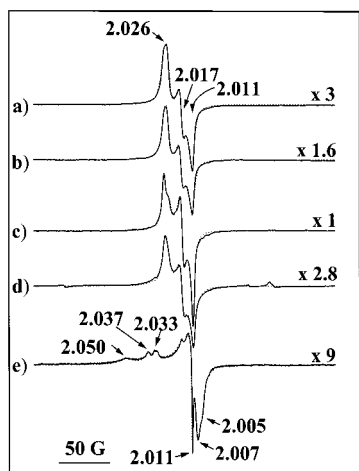


Figure 7. EPR spectra following O_2 adsorption at 77 K on (a) 1CA, (b) 2CA, (c) 10CA, (d) 39CA, and (e) C samples. Computer-simulated spectra are overlapped as thinner dotted lines.

that the structure of the main peaks is a consequence of the mixed valence of the CeO_2 material in the final state, originating from the hybridization of Ce 4f and O 2p states in the initial state.^{19,20} This final state has, thus, two main components; one of them has one electron in the Ce(4f) level and one hole in the O(2p) band and is split in two sublevels, due to the influence of the ligand field on the Ce(5d) level containing the excited electron, so the B and C peaks correspond to having that electron in states with, respectively, t_{2g} and e_g symmetry, the latter being more stable in the cubic coordination of Ce in CeO_2 . The other component, giving rise to peak A, has no electron in the Ce(4f) level and no hole in the O(2p) levels; the crystal field effects on the Ce(5d) orbitals containing the excited electron remain here unresolved. Peak D has been found to arise from transitions to the bottom of the conduction band.²⁰

Overall, sample 2CA presents a XANES shape very similar to the CeO_2 reference; in particular, the two mixed valence contributions appear in similar proportions, implying clearly a Ce^{4+} state. Some subtle differences appear, however, in a more thorough analysis. First, peaks B and C seem to collapse, yielding a single maximum at a position $E \approx 5727$ eV, noticeably displaced to lower energy in comparison to the average position of the corresponding features in CeO_2 ; second, the first CR is observed at $E \approx 5765$ eV, i.e., shifted ca. 2.6 eV to lower energy with respect to the CeO_2 reference.

EPR. Figure 7 shows EPR spectra after oxygen adsorption (see Experimental Section for procedure description) on the samples outgassed at 773 K. On the basis of computer simulations, the spectra are formed by the overlapping of different signals, in agreement with previous results on similar samples;^{11,15,21} their characteristics are shown in Table 2.

In the case of alumina-supported samples, the spectra are mainly formed by the overlapping of signals OCA1 and OCA2.

TABLE 2: Characteristics^a of the EPR Signals Ascribed to $Ce^{4+}-O_2^-$ (see text) Obtained upon Oxygen Adsorption on the outgassed Samples

signal	EPR parameters	proposed adsorption sites
OCA1	$g_{\perp} = 2.026$, $g_{\parallel} = 2.012$	Ce ions at the edges of 2D-Ce patches on alumina
OCA2	$g_z = 2.028-2.027$, $g_x = 2.017$, $g_y = 2.011$	Ce ions at the surface of 2D-Ce patches on alumina
OC1	$g_z = 2.035-2.033$, $g_x = 2.012-2.011$, $g_y = 2.010$	isolated oxygen vacancies at the surface of ceria particles
OC2	$g_z = 2.037$, $g_y = 2.012$, $g_x = 2.007$	associated oxygen vacancies at the surface of ceria particles
OC3	$g_z = 2.050$, $g_y = 2.010$, $g_x = 2.005$	associated oxygen vacancies at the surface of ceria particles
OC4	$g_z = 2.031$, $g_x = 2.017$, $g_y = 2.011$	isolated oxygen vacancies at the surface of ceria particles, probably influenced by impurities

^a Obtained by computer simulation of the spectra. ^b More details for axis attributions can be found elsewhere.^{15,21}

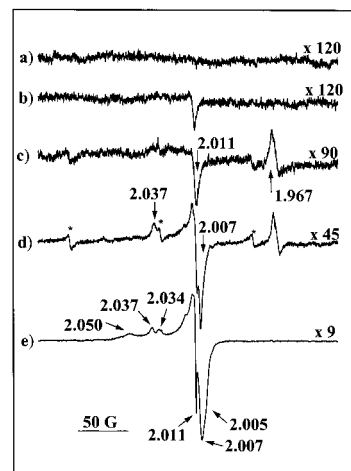


Figure 8. Same as Figure 7 after subsequent outgassing at room temperature. Asterisks correspond to Mn^{2+} impurities.

For samples with CeO_2 loadings ≥ 2 wt %, inclusion of minor contributions of signals OC1 and/or OC2 is required to obtain satisfactory simulations. These latter signals are best revealed when the treatment giving rise to the spectra of Figure 7 is followed by outgassing of the samples at room temperature, leading to the disappearance of signals OCA1 and OCA2 (Figure 8). These latter spectra show the presence of signal OC1 for samples 2CA, 10CA, and 39CA (it may be that it is also present for sample 1CA but, if so, at only a very low level as the $g = 2.011$ position in Figure 8a shows a just barely discernible peak), its intensity increasing upon increasing the amount of CeO_2 , and of signal OC2 for sample 39CA. All of them present rather smaller intensity than the signals OCA1 and OCA2, which were present before this last outgassing and which obscured the OC1 and OC2 components. The spectra of samples 10CA and 39CA also display a sextet of small lines, due to a Mn^{2+} impurity, and a peak at $g = 1.967$, ascribed to bulk defects in the CeO_2 lattice.^{15,21} These signals are not related to the surface chemistry of the samples and will not be further discussed here.

On sample C, oxygen adsorption produces a spectrum (Figure 7e) formed by the overlapping of signals OC1, OC2, OC3, and OC4. The same signals are observed after subsequent outgassing at room temperature; the latter actually produces a small intensity increase, mainly due to increases of signals OC2 and OC3, which is most likely ascribable to the elimination of some nonchemisorbed oxygen (which, considering its paramagnetic character, can cause broadening and amplitude decrease in the spectra by magnetic interactions) still present in the EPR cell.

Signals OC1, OC2, OC3 and OC4 are ascribed (using formal charges) to $Ce^{4+}-O_2^-$ species, on the basis of previous detailed oxygen adsorption experiments including use of ^{17}O -enriched oxygen mixtures.²¹ These can be assumed to be formed by electron transfer to O_2 from the ceria surface, their intensity giving thus a measure of the degree of surface reduction.

Differences between the signals are attributed to changes in the chemical environment of the Ce sites, where oxygen is chemisorbed. On the basis of the more severe thermal pretreatments required for the formation of those $\text{Ce}^{4+}-\text{O}_2^-$ species, their relatively higher line width, and the specific reactivity for NO decomposition shown by the cerium-(anion vacancy) centers where they are formed,⁵ signals OC2 and OC3 are attributed to $\text{Ce}^{4+}-\text{O}_2^-$ species generated at centers containing associated oxygen vacancies. On the contrary, signals OC1 and OC4 have been ascribed to $\text{O}_2^--\text{Ce}^{4+}$ species formed at isolated oxygen vacancy centers.²¹ It is worth mentioning that the presence of associated vacancy centers (whose formation would not be thermodynamically favored until a sufficiently large amount of isolated vacancies would have been created)²² in mildly reduced ceria has been demonstrated by STEM²³ and justified by computer simulations.²⁴

Signals OCA1 and OCA2, on the other hand, are exclusively produced in alumina-supported ceria samples. According to previous works using ^{17}O -enriched oxygen mixtures,^{15,25} they are also due to $\text{O}_2^--\text{Ce}^{4+}$ species. However, the significant differences between their g values and those observed for signals OC1–OC4 (which are clearly revealed by the different shapes observed when comparing the spectra of $x\text{CA}$ samples and sample C, Figure 7) must be attributed to changes in the coordination environment of the corresponding centers. In the present case, and considering the short range of the interactions which determine the g -tensor values in these species,²⁶ type-OCA signals must be attributed to $\text{O}_2^--\text{Ce}^{4+}$ species involving cerium ions which are highly dispersed on the alumina surface.

As shown in previous works using ^{17}O -enriched oxygen mixtures, the g_x value of $\text{O}_2^--\text{Ce}^{4+}$ species (by convention, the one in which the highest ^{17}O -hyperfine splitting is centered)^{25,26} is significantly shifted from g_e (free electron g value = 2.0023).^{15,21,25} Taking into account that ionically bonded superoxide species show g_x values very close to g_e ,²⁶ this shift has been attributed to the partially covalent character of the $\text{O}_2^--\text{Ce}^{4+}$ bond involving some participation of the 4f Ce orbital;^{21,25} well-defined examples of similar cases in other complexes of this kind can be found elsewhere.²⁶ Then, the higher g_x shift of type-OCA signals with respect to type OC signals indicates an even higher covalent character in the former complexes.

Figure 9 shows the overall amount of $\text{Ce}^{4+}-\text{O}_2^-$ species detected in the experiments of Figure 7, plotted as a function of the ceria loading and separated in contributions from signals due to alumina-modified dispersed cerium species (sum of OCA1 and OCA2) and those formed on aggregated ceria (signals OC1–OC4). While the former reaches a maximum for sample 10CA, with sample 39CA showing a smaller amount similar to that yielded by sample 1CA, the overall contribution of type-OC signals shows a monotonic increase with the amount of ceria. On the other hand, the OCA2/OCA1 intensity ratio shows as well a maximum for sample 10CA, as also displayed in Figure 9.

It is important to note that exactly the same signals OCA1 and OCA2 are observed (on the basis of computer simulation evidence) for all the alumina-supported ceria samples, in the whole ceria compositional range. Small differences in these signals between the different samples concern exclusively their line widths, which can slightly change from one sample to another (in the range $\langle D \rangle = 4\text{--}2$ G, where $\langle D \rangle$ is the average line width) with no clear trend having been observed. These changes in width may be due merely to small variations in the amount of residual nonchemisorbed oxygen present in each case.

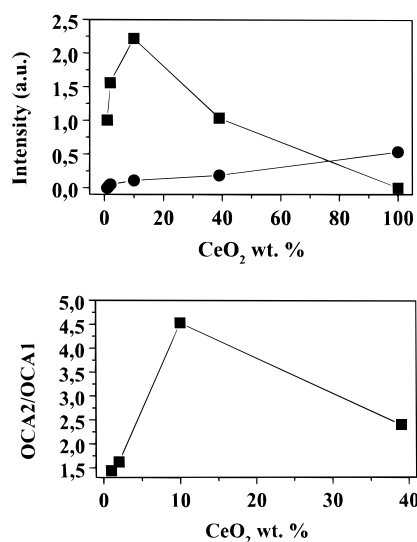


Figure 9. Overall intensity of EPR signals type OCA (squares) and OC (circles), as deduced from computer simulations of the spectra in Figure 7, with respect to the ceria loading of the samples (upper part) and OCA2/OCA1 intensity ratio deduced from computer simulations of the spectra of Figure 7 vs ceria loading (lower part).

To verify that these effects are not affecting the observed results, sample 10CA has been subjected to outgassing at 77 K during increasing time intervals following an initial O_2 adsorption at 77 K; the results (not shown) have shown that, even though overall line widths decrease from $\langle D \rangle \approx 7$ G to $\langle D \rangle \approx 2$ G, only ca. 5–10% increases in the overall integrated intensity were found, with no important changes in the OCA2/OCA1 ratio.

Discussion

The XRD, Raman, and TEM-electron diffraction data (Figures 1–4) clearly show that, as could be expected, ceria particles with a well-formed fluorite structure appear in increasing amounts upon increasing the cerium content in $x\text{CA}$ samples; their average size also shows the same trend. However, the increase in the amount of this phase is clearly not linear with the Ce load. This is indicated by the Raman results, even if they are utilizable only at a semiquantitative level. On the other hand, TEM results on the highest loaded sample (39CA) show a large predominance of ceria particles, as these are observed even in Al-enriched zones ($\text{Ce}/\text{Al} = 6 \times 10^{-3}$) similar to those characteristic of 2CA, in strong contrast with the absence of these features for the latter sample. These results indicate that, below a certain ceria content, the formation of ceria particles is relatively damped, in favor of formation of dispersed ceria species, the opposite occurring above that breakpoint. Results in the same line have been observed by other authors in related materials on the basis of Raman and XPS.¹³

Failure to detect these particles by the above-mentioned techniques for samples 1CA and 2CA does not exclude, however, that they could be present with sizes lower than ca. 1 nm, which is estimated to be the detection limit of the TEM technique here employed. Indeed, EPR results (Figure 8) indicate the presence of signals similar to those observed for unsupported ceria (type-OC signals) in sample 2CA, thus indicating that this sample can indeed contain some amount of 3D-Ce, which must in any case be very small. The absence of features due to those smaller particles in the XRD, Raman, or TEM results must be due to the lower detecting power of these techniques, with respect to EPR, or to the loss of crystallinity which is expected, on the basis of theoretical calculations, to be experienced by

ceria particles below ca. 1 nm in size.²⁷ Thus, the absence of ceria-related features in the results of these techniques indicates indirectly that ceria must be present in a highly dispersed state at least in the samples with lower Ce content.

In contrast, the presence of such a dispersed ceria component, invisible for the diffraction and Raman techniques, is clearly revealed in the EPR experiments by the presence of type-OCA signals. As noted before, the short range of the interactions determining the EPR features of these signals indicates that the cerium ions, where those superoxide species are formed, must be in direct contact with the alumina surface. This leaves as possible explanations for this dispersed ceria component the presence of two-dimensional ceria patches (2D-Ce) and/or of isolated cerium ions, both possibilities having been also pointed out by previous investigations.¹⁵ However, the absence of sharper features in the UV-vis DRS spectra of α CA samples (Figure 5) points toward the absence of a significant amount of such isolated ions in these samples.¹⁸ Thus, the dispersed ceria component in α CA samples is most likely formed by two-dimensional ceria patches.

Characteristics of 3D-Ce Particles. As noted above, the EPR data in Figure 8 show that type-OC signals, and therefore 3D-Ce species, appear already for the 2CA sample, even though the small amplitude found in that case implies that the corresponding fraction of cerium is very small. A larger amount of such particles does exist in 10CA. Particularly interesting is the fact that, among the OC-type signals, those ascribed to associated vacancy centers only appear, within α CA samples, for the 39CA material. Thus, it seems that the surfaces of the small ceria particles present in sample 10CA (and also in the less loaded specimens) do not yet develop the full chemical behavior of a well formed ceria phase.

This surprising observation is not merely due to particle size effects, since EPR data on O₂ adsorption indicate that both kinds of vacancy centers appear in a pure ceria material which has a particle size (ca. 3 nm, on the basis of TEM) even lower than that observed for the ceria particles present in sample 10CA.²⁸ Furthermore, it has been claimed that smaller particles should be more easily reducible,²⁷ so that these would be expected to accumulate a higher concentration of anion vacancies for the same outgassing treatment.

To explain this, it may be taken into account that, as indicated by atomistic simulations,²⁴ ceria particles exposing different crystallographic planes may differently favor the association of vacancies formed on them. According to those simulations, such association would be favored on (111) planes (and so has been observed experimentally by STM)²³ but not on (110) planes. Thus, it may occur that only the larger particles, as they appear on sample 39CA, develop the favorable surface planes, while for Ce contents as in sample 10CA and below the particle growth mode leads mainly (at least with the present preparation method) to the presence of planes not favorable for vacancy association. This suggests an influence of some epitaxy between ceria and the underlying alumina. It could be that the different proportions between amplitudes of the (111) and (311) electron diffraction lines observed within profiles d-f of Figure 3 were due to such epitaxial effects, but these data are too limited to justify a thorough discussion in this respect.

In any case, it is worth noting that differences in the ability for creating those associated vacancy centers, which may result from different cerium contents and/or different growth modes of ceria particles on alumina, may have important consequences for chemical and catalytic properties. Previous work has shown, for example, that reaction of NO with a CeO₂ surface to form N₂O already at room temperature occurs on associated anion

vacancies, not on isolated ones.⁵ Also, significant differences in catalytic activity for CO oxidation have been recently shown for palladium catalysts supported on α CA samples or on pure ceria (the former being much more active).²⁹ In view of the results presented here, it might be that the deactivation observed for the ceria-supported catalyst, which according to IR data could be due to oxidation of the palladium particles in contact with unsupported ceria, was related to the different ease of formation of associated vacancies or at least to the different type of ceria surfaces exposed. It is also worth noting that even smaller differences in the redox behavior between ceria particles present in 39CA and unsupported ceria are revealed by formation of only one kind of associated vacancies centers (giving rise to signal OC2) upon outgassing in the former case.

Characteristics of 2D-Ce Entities. As noted above, observation of type-OCA signals in the EPR spectra of α CA samples indicates the presence of 2D-Ce entities. Furthermore, the same OCA signals are observed in all these samples, which indicates that the 2D-Ce entities must possess rather similar characteristics in all of them. The fact that a maximum of these signals is observed for sample 10CA, decreasing for sample 39CA to a value similar to that found for 1CA, agrees with the previously mentioned large predominance of 3D-Ce entities in 39CA.

Since two OCA-type signals are observed, which differ in the g_x value, and the deviation of the latter from g_e is ascribed to covalency effects due to the presence of Al in the neighborhood of the Ce ions, the most straightforward explanation for the presence of types of two such species implies that the relative proportions of ceria-like and alumina-like environments around the Ce cation is different in both types. Then, it may be presumed that signal OCA1 (having the largest g_x , actually $g_x = g_z = 2.026$) corresponds to Ce ions at the periphery of the 2D-patches, while signal OCA2 would be due to species at the surface of those patches. Indeed, their proportions vary in agreement with this model: the OCA2/OCA1 ratio is lowest for the samples with lowest Ce load, in which the patches are expected to be smallest and their periphery-to-surface ratio to be highest. It is noteworthy that this ratio falls again for sample 39CA, indicating that the 2D-Ce patches remaining here are very small, possibly of a size insufficient to promote further growth into 3D-Ce particles.

Some additional information on those Ce ions lying in the 2D-Ce entities can be drawn from the XANES spectra in Figure 6. In this case, the spectrum is taken from a specimen in which the contribution of 3D-Ce particles is negligible, so that the features observed will be representative of the well-dispersed Ce ions present in two-dimensional ceria species.

First, the presence in the XANES spectrum of 2CA of a "white line" composed of two main peaks with similar intensity, as in pure CeO₂, confirms that these ceria species highly dispersed on alumina, formerly described¹³ as "precursors" of the CeAlO₃ phase (which contains Ce³⁺), are undoubtedly in the tetravalent state, quite as in CeO₂. Subtle differences between samples 2CA and CeO₂ give, however, some interesting information. In first place, the splitting between peaks B and C observable in CeO₂ cannot be resolved in sample 2CA, which presents instead a single peak in that position. The shape and width of this latter spectral feature suggest that this difference is not due to a broadening of the spectrum components, as might well happen in this not so well-defined material. Rather, the separation between the component peaks seems to have decreased, indicating that the splitting between the e_g and t_{2g} manifolds in the 5d level containing the excited electron has decreased. Thus, the crystal field on the Ce ions seems to be

lower in the 2CA sample. Second, the average position of the (B + C) feature is located in sample 2CA at an appreciably lower energy than in pure CeO_2 . Such peak displacement does not seem to have occurred to a similar extent for feature A. To analyze this observation, one must recall that the (B + C) feature corresponds to a final state which has an electron in the Ce 4f level and a hole in the O 2p band, while in the final state corresponding to feature A there is no electron in the 4f level and the O 2p band is full. The lower position of the (B + C) features in the spectrum thus suggests that the 4f level of the excited Ce ion is located at lower energy in the 2CA sample than in CeO_2 . On the other hand, the invariance in the position of peak A indicates that the 5d level does not seem to be perturbed to a similar extent. Although these results cannot be easily explained, they are most likely related to a combination of differences, with respect to pure ceria, in factors such as the number, symmetry, distances, and/or net charge (the latter due to their sharing with the alumina) of anion ligands. A decrease in Madelung potential due to the small ceria particle size might also contribute here. These changes, in turn, will induce electrostatic as well as chemical effects in the electronic configuration of the Ce cations. Whichever is the precise explanation, it is here relevant to stress that the decrease in ligand field may lead to a lower stabilization of higher oxidation states of the Ce cations, i.e., to a higher stabilization of the higher electronic levels in the latter.

Finally, one may observe in the XANES spectrum of 2CA that the continuum resonance appearing around 5727 eV is weaker and red-shifted with respect to the similar feature in sample C. Since this CR depends mainly on second and third neighbors, not on the directly contacting anion ligands, and the 2D-Ce patches are of limited size, this observation suggests that the nearest Ce neighbors in the 2D-Ce entities are located at somewhat longer distance than in CeO_2 . It is noted that an electronic effect (of a modified coordination) could also influence the CR position. However, the large magnitude of the shift (2.6 eV) cannot be accounted for exclusively on this basis. Thus, the "expansion" of interatomic distances in the surface ceria patches, possibly related to epitaxial effects, is certainly one of the causes of ligand field decrease.

Thus, the XANES data indicate in more than one way that the highly dispersed cerium species present in the 2D-Ce patches experience, even in a nonoutgassed sample (thus expected to be fully hydroxylated), a decreased interaction with the neighboring oxide anions in comparison with that occurring in CeO_2 . The stabilization of highly charged cations will thus be smaller. This explains that the amount of reduced centers formed by a given outgassing treatment (which is a measure of the ceria reducibility) is significantly higher on those patches than on better developed 3D-Ce particles; this is easily seen by comparing the respective signal intensities obtained in the EPR spectra (Figure 9). Actually, the cerium ions at the periphery of such patches, in which the deviation from the situation in pure ceria is the highest, are the easiest to reduce, as verified in previous work, where the corresponding EPR signal OCA1 was formed first for the lowest outgassing temperatures.¹⁵ The stabilization of the empty 4f orbitals allows us to rationalize also the larger covalent character of the O_2^- -Ce bond, as a higher amount of electron density from the superoxide radical will be delocalized onto them. Or, expressed in other terms, the transfer of electron density from the initial Ce^{3+} ion to the O_2 molecule is less complete because it leads to a less important decrease in energy. This explains additionally the fact that oxygen desorption from these centers, which occurs with

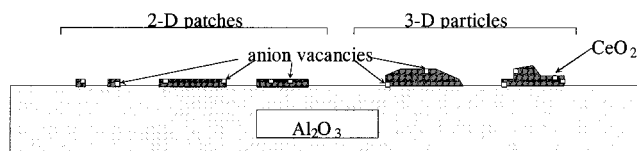


Figure 10. Proposed model for ceria entities present in alumina-supported ceria samples showing possible locations for vacancies generated by reduction.

concomitant back-transfer of electrons to the surface, is so easy (produced by simple outgassing at room temperature, compare Figures 7 and 8). And finally, it explains the higher difficulty in reoxidizing the Ce^{3+} centers formed upon reduction of 2D-Ce entities, as observed in previous works:¹⁵ the electron in that cation is more stable and difficult to take out, and furthermore, the O_2^- radical, with part of its electron density delocalized from its antibonding HOMO over the Ce ion, will have a O—O bond which is stronger (leading to a higher stretching vibrational frequency, as observed by IR spectroscopy)¹⁵ and harder to break.

Concluding Remarks

As a summary of the results obtained, a complete model on the characteristics of ceria entities in these alumina-supported ceria samples can be proposed, as shown in Figure 10. Samples 1CA, 2CA, and 10CA present increasing amounts of all types (2D or 3D) of ceria particles epitaxially grown on the alumina surface; specifically, 2D-Ce entities (initially the dominant ones) show sizes increasing with the cerium content of the samples (for weight percent ≤ 10). These 2D-Ce patches contain Ce as Ce^{4+} (and not Ce^{3+} as in CeAlO_3) with relaxed coordination distances and experience a decreased ligand field which leads to higher reducibility of the cation, more covalent O_2^- - Ce^{4+} bond, and lower oxygen adsorption energy in this surface complex. On the other hand, cerium oxide entities in sample 39CA are constituted mainly by 3D-Ce particles. The large development of some of these particles in this sample allows them to present a chemical behavior more similar to that observed for unsupported ceria, in contrast with similar 3D-Ce species observed in samples 10CA or with lower ceria loading, in which association of surface anion vacancies is hindered. However, even in the case of 3D-Ce particles present in 39CA, there appear small differences in the chemical (redox) behavior in comparison with unsupported ceria, as evidenced by formation of only one kind of associated vacancies centers (giving rise to EPR signal OC2) in sample 39CA. It is noteworthy that EPR allows one to show chemical differences between these various ceria species.

On the basis of these interpretations, important questions are open concerning the molecularly designed preparation of TWCs. Depending on which are the most optimum metal-promoter interactions for a given reaction, i.e., which are the optimal ceria sites onto which it is worthier to apply the metallic component in order to obtain maximum catalytic activity, it will be convenient to devise the deposition of ceria over the alumina carrier differently. Examination by EPR of the supports may shed significant light on the adequacy of each ceria/alumina material for the desired application. Some work in our laboratory has been devoted to this aspect, focusing on the CO oxidation reaction. It was shown that the optimum configurations depend on the nature of the metal deposited on the sample; for instance, the most active copper species are formed upon interactions with independent ceria particles,⁹ while most active palladium

species are apparently formed on alumina-affected ceria particles.²⁹

Finally, it is worth noting that similar results can be expected to be obtained in the case that Zr–Ce mixed oxides (which are claimed to constitute the promoting component in new generation TWC's),³⁰ instead of ceria, are deposited on alumina, considering the large similarities between the characteristics of both oxides. Work is in progress in our laboratory in order to study those materials.

Acknowledgment. Financial support by projects from CA-ICYT (No. MAT 97-0696-C02-01) and CAM (No. 06M/084/96) is acknowledged. Prof. E. Martínez Tamayo is greatly acknowledged for preparation of the CeAlO₃ reference sample and Dr. V. Cortés Corberán is also thanked for advice on this. Thanks are also due to the BM29 staff for recording the XANES spectra (obtained under the Rapid Access XAFS facility). Mrs. M. Garrido and Dr. M. Faraldos are thanked for recording the X-ray diffractograms and DRS spectra, respectively. A. M.-A. and M. F.-G. wish to thank, respectively, the Comunidad Autónoma de Madrid and the CSIC for postdoctoral grants or contracts under which this work has been carried out.

References and Notes

- (1) Trovarelli, A. *Catal. Rev. Sci. Eng.* **1996**, 38, 439 and references therein.
- (2) (a) Dictor, R.; Roberts, S. *J. Phys. Chem.* **1989**, 93, 5846. (b) Su, E. C.; Rothschild, W. G. *J. Catal.* **1986**, 99, 506.
- (3) (a) Yao, H. C.; Yu Yao, Y. F. *J. Catal.* **1984**, 86, 254. (b) Engler, B.; Koberstein, E.; Schubert, P. *Appl. Catal.* **1989**, 48, 71. (c) Miki, T.; Ogawa, T.; Haneda, M.; Kakuta, N.; Ueno, A.; Tateishi, S.; Matsuura S.; Sato, M. *J. Phys. Chem.* **1990**, 94, 6464.
- (4) (a) Shido, T.; Iwasawa, Y. *J. Catal.* **1992**, 136, 493. (b) Shido, T.; Iwasawa, Y. *J. Catal.* **1993**, 141, 71.
- (5) Martínez-Arias, A.; Soria, J.; Conesa, J. C.; Seoane, X. L.; Arcoya, A.; Cataluña, R. *J. Chem. Soc., Faraday Trans.* **1995**, 91, 1679.
- (6) Hardacre, C.; Ormerod, R. M.; Lambert, R. M. *J. Phys. Chem.* **1994**, 98, 10901.
- (7) Zafirios, G. S.; Gorte, R. J. *J. Catal.* **1993**, 139, 561.
- (8) Martínez-Arias, A.; Soria, J.; Conesa, J. C. *J. Catal.* **1997**, 168, 364.
- (9) Martínez-Arias, A.; Soria, J.; Cataluña, R.; Conesa, J. C.; Cortés Corberán, V. *Stud. Surf. Sci. Catal.* **1998**, 116, 591.
- (10) Martínez-Arias, A.; Cataluña, R.; Conesa, J. C.; Soria, J. *J. Phys. Chem. B* **1998**, 102, 809.
- (11) Martínez-Arias, A.; Coronado, J. M.; Cataluña, R.; Conesa, J. C.; Soria, J. *J. Phys. Chem. B* **1998**, 102, 4357.
- (12) Van Yperen, R.; Lindner, D.; Mubmann, L.; Lox, E. S.; Kreuzer, T. *Stud. Surf. Sci. Catal.* **1998**, 116, 51.
- (13) Shyu, J. Z.; Weber W. H.; Gandhi, H. S. *J. Phys. Chem.* **1988**, 92, 4964.
- (14) Zaki, M. I.; Hussein, G. A. M.; Mansour, S. A. A.; Ismail, H. M.; Mekhemer, G. A. H. *Colloids Surf. A* **1997**, 127, 147.
- (15) Soria, J.; Coronado, J. M.; Conesa, J. C. *J. Chem. Soc., Faraday Trans.* **1996**, 92, 1619.
- (16) Bensalem, A.; Bozon-Verduraz, F.; Delamar, M.; Bugli, G. *Appl. Catal. A* **1995**, 121, 81.
- (17) Morterra, C.; Bolis, V.; Magnacca, G. *J. Chem. Soc., Faraday Trans.* **1996**, 92, 1991.
- (18) Bensalem, A.; Muller, J. C.; Bozon-Verduraz, F. *J. Chem. Soc., Faraday Trans.* **1992**, 88, 153.
- (19) El Fallah, J.; Boujana, S.; Dexpert, H.; Kiennemann, A.; Majarus, J.; Touret, O.; Villain, F.; Le Normand, F. *J. Phys. Chem.* **1994**, 98, 5522.
- (20) Soldatov, A. V.; Ivachenko, T. S.; Della Longa, S.; Kotani, A.; Iwamoto, Y.; Bichcom, A. *Phys. Rev B* **1994**, 50, 5074.
- (21) Soria, J.; Martínez-Arias, A.; Conesa, J. C. *J. Chem. Soc., Faraday Trans.* **1995**, 91, 1669.
- (22) Sørensen, O. T. *Nonstoichiometric oxides*; Academic Press: New York, 1981; p 17.
- (23) Nöremberg, H.; Briggs, G. A. D. *Phys. Rev. Lett.* **1997**, 79, 4222.
- (24) Conesa, J. C. *Surf. Sci.* **1995**, 339, 337.
- (25) Martínez-Arias, A.; Coronado, J. M.; Conesa, J. C.; Soria, J. In *Rare Earths*. Sáez Puche, R., Caro, P., Eds.; Editorial Complutense: Madrid, 1997; p 299.
- (26) Che, M.; Tench, A. J. *Adv. Catal.* **1983**, 32, 1.
- (27) Cordatos, H.; Ford D.; Gorte, R. J. *J. Phys. Chem.* **1996**, 100, 18128.
- (28) Martínez-Arias, A. Unpublished results.
- (29) Fernández-García, M.; Martínez-Arias, A.; Salamanca, L. N.; Coronado, J. M.; Anderson, J. A.; Conesa, J. C.; Soria, J. *J. Catal.* **1999**, 187, 474.
- (30) Vlaic, G.; Di Monte, R.; Fornasiero, P.; Fonda, E.; Ka?par, J.; Graziani, M. *J. Catal.* **1999**, 182, 378.